AVERAGE CROSS-SECTIONAL AREA OF IDEALIZED DEBRISAT FRAGMENTS USING ICOSAHEDRON MOTIVATED ORIENTATION VECTORS

Thomas Scruggs[(1)], Norman Fitz-Coy[(2)]

[(1)] *University of Florida, Gainesville, FL, USA 32611, Email: scruggsta@ufl.edu*
[(2)] *University of Florida, Gainesville, FL, USA 32611, Email: nfc@ufl.edu*

ABSTRACT

Debris fragments from the hypervelocity impact testing of DebriSat are being collected and characterized for use in updating existing satellite breakup models. One of the key parameters utilized in these models is the ballistic coefficient of the fragment which is directly related to its area-to-mass ratio. By definition the area in the ratio is the cross-sectional area perpendicular to the direction of motion. However, since the attitude of fragments can vary during their orbital lifetime, it is customary to use the average cross-sectional area in the calculation of the area-to-mass ratio. The average cross-sectional area is defined as the average of the projected surface areas and has been shown to be equal to the one-fourth of the total surface area of a convex object.

An 3D imaging system was developed for use in determining the size characteristics (i.e., characteristic length) of the DebriSat fragments. The 3D imaging system consists of six cameras at equally spaced elevation angles, which means the resulting camera orientation vectors are not evenly spaced on the hemisphere above the fragment while it is imaged. This leads to the need for a weighting factor associated with the projected areas measured by the cameras. This paper investigates a notional imaging system where the orientation vectors of the cameras are inspired by the vertices of an icosahedron. An icosahedron is a platonic solid, which means the vertices of an icosahedron are evenly spaced from each other. Also, this paper explores the subdivided icosahedron for additional camera orientation vectors to improve the calculation of the average cross-sectional area of various objects. Finally, orientation vectors of the notional system are used to motivate a weighting factor for the existing 3D imaging system; that is, particular images from the 3D imaging system are weighted to approximate orientations from the notional system.

1 INTRODUCTION

The study of space debris remains an active area of research due to potential complications posed by space debris. It has been shown that debris fragments down to a size of 1 cm can cause catastrophic damage to space missions [1]. Additionally, a catastrophic collision between satellites has far-reaching effects due to the potential for subsequent collisions, which could result in the exponential growth of debris fragments (known as the Kessler effect) [2]. Therefore, accurate mapping of space debris is critical to prevent growth in the number of debris. In low Earth orbits (LEOs), larger debris fragments can be tracked with ground-based methods, but a number of debris fragments are too small to be tracked from the ground [3].

DebriSat is a joint project between the National Aeronautics and Space Administration (NASA), the United States Air Force/Space and Missile Systems Center (USAF/SMC), The Aerospace Corporation, and the University of Florida (UF) to update the existing NASA and Department of Defense (DOD) standard breakup model for satellite debris fragments. The current standard breakup model is based on a Navy transit satellite that was fabricated in the 1960's. After the accidental collision between the Iridium-33 satellite and retired Cosmos-2251 satellite in 2009, the need to update the standard breakup model was reinforced. The debris generated by the older Cosmos-2251 was accurately modeled by the standard breakup model, but the model under predicted debris from the newer Iridium-33 satellite [4]. The under prediction of the fragments from the Iridium-33 has been attributed to the use of new materials and technologies in its fabrication. To make the necessary updates to the standard breakup model a representative LEO satellite was fabricated and subjected to a hypervelocity impact. Processing and characterization efforts of the debris from the impact are ongoing at UF [4].

One key parameter of the standard breakup model is the fragment's ballistic coefficient since ballistic coefficient is used in determining the orbit lifetime of the fragment. The ballistic coefficient of the fragment is directly related to its area-to-mass ratio, where the area is the cross-sectional area of the fragment perpendicular to the direction of motion. However, since the attitude of the fragment can vary during its orbital lifetime, it is customary to use an average cross-sectional area (ACSA) to calculate the fragment's ballistic coefficient. Average cross-sectional area is defined as the average projected surface areas of an object viewed from 4π steradians [5]. In the earliest documented study of

average cross-sectional area (referred to as average projected area) of three-dimensional (3D) objects, Cauchy proved that the average projected area of a convex object is one-fourth of the object's total surface area [5]. Currently, ACSA of debris fragments is approximated in the satellite standard breakup model based on categorization of the fragments as either irregular or plate-like [6]. The ACSA approximations for irregular and plate-like classified fragments are given by Eq. 1 and Eq. 2, respectively. In these approximations, x is the longest dimension of the fragment, y is the longest dimension orthogonal to x, z is the longest dimension orthogonal to both x and y, and L_C is the arithmetic mean of x, y, and z.

$$ACSA_{irregular} = \frac{2}{9}(x \cdot y + y \cdot z + z \cdot x) \qquad (1)$$

$$ACSA_{plate} = \frac{1}{2}(L_C^2 + 2L_C \cdot z) \qquad (2)$$

However, it has been shown that these models can produce large errors [6]. One aspect of the DebriSat project, explored in this paper, is to improve the calculation of ACSA of the debris fragments.

In previous work on the DebriSat project, a 3D imaging system was developed to determine size characteristics of the fragments [7]. The 3D imaging system consists of six cameras (labeled A-F) at increasing elevation angles directed towards a turntable as shown in Fig. 1.
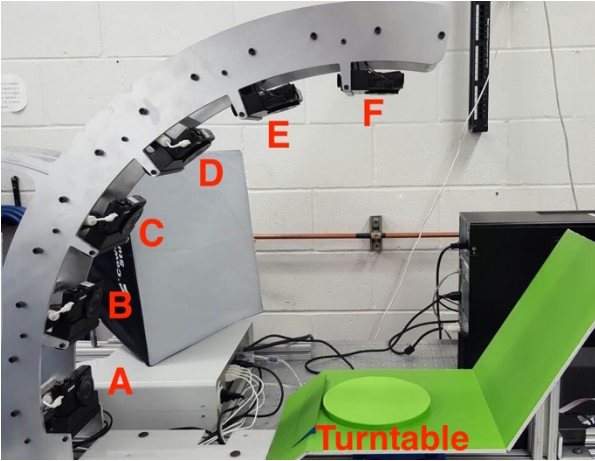

Figure 1. 3D imaging system

Fragments are placed on the turntable, which incrementally rotates while the fragment is imaged by the cameras. A turntable increment is defined as the number of equal rotations for the turntable to rotate a full 360°. Each image represents a projected area from an orientation vector that points from the camera to the object. A previous study utilized these projected areas recorded by the 3D imaging system to calculate the ACSA of test objects [8]. However, as shown in [8], the orientation vectors associated with the projected areas

recorded with the 3D imaging system are not equally spaced around the object. This led to the need for the projected areas to be weighted when calculating ACSA. If the projected areas of the object were equally distributed around the object a weighting factor would be unnecessary when calculating ACSA.

This paper investigates one way to generate projected areas of an object whose respective orientation vectors are equally distributed. The orientation vectors are inspired by a regular icosahedron, shown in Fig. 2, which is one of the five platonic solids.
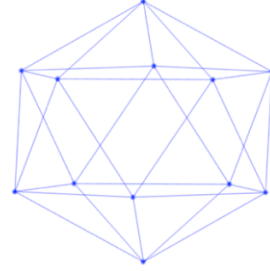

Figure 2. Regular icosahedron

This paper is organized as follows: Section 2 describes calculating ACSA with a notional icosahedron-inspired imaging system where the orientation vectors correspond to the vertices of a regular icosahedron. Section 3 explores subdividing the edges of the icosahedron to generate additional orientation vectors. Section 4 uses the insight from the icosahedron-inspired imaging system to formulate a weighting factor that is then applied to an imaging system that emulates the 3D imaging system. In Section 5 the results of applying the weighting factor to images recorded by the 3D imaging system to calculate ACSA are presented as well as concluding remarks. Also, in Section 5 the calculated ACSA is compared to previous results as well as the ACSA model used with the current standard breakup model. Section 6 consists of future works.

2 ICOSAHEDRON-INSPIRED IMAGING SYSTEM

Figure 3 shows a unit orientation vector, $\hat{\boldsymbol{v}}$, defined by its azimuthal angle (ϕ) and polar angle (θ) that points from the observation point (denoted as the asterisk) to the origin of the coordinate system. In the icosahedron-inspired imaging system the observation points are aligned with the vertices of a regular icosahedron. Since the regular icosahedron is a platonic solid, the vertices (and resulting orientation vectors) are equally spaced around the origin of the coordinate system. Table 1 shows the locations of the twelve observation points (P_1-P_{12}) of the icosahedron-inspired imaging system.
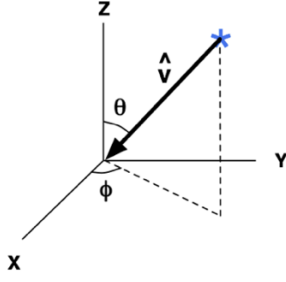
Figure 3. Orientation vector definition

Table 1. Icosahedron-inspired imaging system observation point locations

Observation Point	Polar Angle (θ)	Azimuthal Angle (ϕ)
P_1	0°	0°
P_2	63.44°	0°
P_3	63.44°	72°
P_4	63.44°	144°
P_5	63.44°	216°
P_6	63.44°	288°
P_7	116.57°	36°
P_8	116.57°	108°
P_9	116.57°	180°
P_{10}	116.57°	252°
P_{11}	116.57°	324°
P_{12}	180°	0°

For the notional imaging system, the following convex objects are tested: a sphere of unit radius, a cylinder of unit radius and unit height, a cube with unit edge lengths, an octahedron with unit edge lengths, a square pyramid with unit edge lengths, and a tetrahedron with unit edge lengths. Since the test objects are convex, the true ACSA can be directly computed as one-fourth of the total surface area of the object. Table 2 shows the true ACSAs for the test objects.

Table 2. True ACSA (in unit^2) of test objects

Test Object	True ACSA
Sphere	3.142
Cylinder	3.142
Cube	1.500
Octahedron	0.866
Square Pyramid	0.683
Tetrahedron	0.433

Before the ACSA of the test objects can be computed, the projected area ($A(\theta,\phi)$) of the objects must be accurately represented as a function of ϕ and θ. This is accomplished by representing the test objects by their area vectors. An area vector is the area of the face of the test object multiplied by the unit normal of the face. For example, Fig. 4 shows the unit cube and its respective area vectors.

With each test object represented by its area vectors the projected area ($A(\theta,\phi)$) of the test object from a

particular orientation vector $\hat{v}$ is computed with Eq. 3 where k is the index associated with the total number of faces of the test object.

$$A(\theta,\phi) = \sum_k (-A_k \cdot \hat{v}) \times H\big(sgn(-A_k \cdot \hat{v})\big) \quad (3)$$

In Eq. 3 the minus sign accounts for the orientation vectors being defined in the opposite direction of the surface normal. Also the Heaviside function, defined as $H(x) = \begin{cases} 0 \ if \ x < 0 \\ 1 \ if \ x \geq 0 \end{cases}$, accounts for the area vectors on the opposite side of the test object from the observation vector.
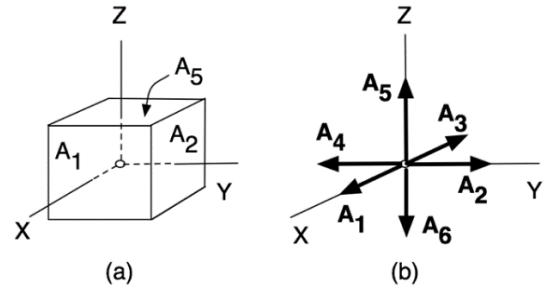

Figure 4. (a) Unit cube and (b) respective area vectors

With the projected areas computed for the twelve orientation vectors of the icosahedron-inspired imaging system, the ACSA is determined by averaging the twelve projected areas. Table 3 shows the percent error of the computed ACSA for the test objects with respect to their true ACSA values. A positive percent error means that the computed ACSA is larger than the true ACSA.

Table 3. Percent error of computed ACSAs

Test Object	Percent Error (%)
Sphere	0.00
Cylinder	1.39
Cube	-1.30
Octahedron	1.48
Square Pyramid	3.82
Tetrahedron	3.32

The zero percent error for the sphere means that the computed ACSA is unbiased since the projected area of a sphere is constant regardless of the orientation of the orientation vector. A comparison of the results shown in Table 3 with those in [8] shows promise for computing the ACSA without a weighting factor since similar errors require at least twice as many observation vectors in the ideal case [8]. This motivates a desire to increase the number of orientation vectors to investigate if the magnitude of the percent errors for the computed ACSAs will decrease similar to the trends displayed in [8].

3 SUBDIVIDED ICOSAHEDRONS

One method to increase the number of orientation vectors that remain nearly evenly distributed is subdividing the twenty equilateral triangles that make up a regular icosahedron as described in [9]. After the triangles have been bisected, the new vertices are normalized to ensure that all of the observation points lie on a unit sphere. Fig. 5 is the observation points of the icosahedron after one subdivision, referred to as a level 1 icosahedron where the regular icosahedron is referred to as a level 0 icosahedron.
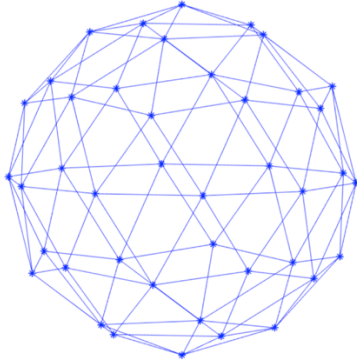

Figure 5. Level 1 icosahedron observation points

After subdivision, the number of orientation vectors increases from 12 to 42. Table 4 shows the percent errors of the computed ACSAs for the orientation vectors associated with the and level 1 icosahedron as well as the previous results.

Table 4. Percent error of computed ACSAs for level 0 and level 1 icosahedrons

Test Object	Level 0 Percent Error (%)	Level 1 Percent Errors (%)
Sphere	0.00	0.00
Cylinder	1.39	-2.24
Cube	-1.30	-2.32
Octahedron	1.48	0.10
Square Pyramid	3.82	-1.27
Tetrahedron	3.32	-0.89

Overall, Table 4 shows no significant improvements in the errors for most of the test objects. In fact, the magnitude of the percent error increases for the cylinder and cube.

One potential cause for the increased magnitude of the percent error can be attributed to the fact that the orientation vectors of the level 1 icosahedron are not equally distributed, but the projected areas are all weighted equally. When the edges of the icosahedron are bisected the new vertices are equidistant from each other, but the new vertices are not a unit away from the geometric center of the icosahedron. The vertices are then normalized to a unit length. This causes the distance between a new vertex to a new vertex to be 13% farther than the distance between a new vertex and an original vertex.

To investigate the trends seen by increasing from a level 0 to a level 1 icosahedron, the edges of the level 1 icosahedron are subdivided to form a level 2 icosahedron. Now the number of orientation vectors is increased to 162. Table 5 is the percent error of the computed ACSA from the level 1 and level 2 icosahedron orientation vectors.

Table 5. Percent error of computed ACSAs for level 1 and level 2 icosahedrons

Test Object	Level 1 Percent Error (%)	Level 2 Percent Errors (%)
Sphere	0.00	0.00
Cylinder	-2.24	-0.51
Cube	-2.32	-0.62
Octahedron	0.10	-0.04
Square Pyramid	-1.27	-0.34
Tetrahedron	-0.89	-0.17

As can be seen in Tab. 5, the magnitude of the percent error of the computed ACSA decreases for all of the shapes (except for the sphere). Part of the decreased magnitude of the percent errors can be attributed to the orientation vectors of the level 2 icosahedron being more equally spaced than the level 1 icosahedron. The distance between a new vertex to a level 1 vertex is 3% longer than the distance between two new vertices. These results show promise for calculating ACSA of objects without a weighting factor as long as the orientation vectors are equally distributed.

The main drawback of results presented for the icosahedron-inspired orientation vectors is that to recreate the orientation vectors with a physical system many stationary or mobile cameras would be needed. This would greatly increase the measurement time to determine the ACSA of the thousands of DebriSat fragments when compared to the existing 3D imaging system. However, insight from the icosahedron-inspired orientation vectors is applied in the form of a weighting factor that is first tested with a system that emulates the 3D imaging system.

4 ICOSAHEDRON WEIGHTING FACTOR

As discussed in [8], the projected area of an object from a particular orientation vector is equal to the projected area of the object from the reflection of the orientation vector. Therefore, the geometry of an icosahedron allows for the twelve orientation vectors of the level 0 icosahedron to be replicated with a two camera system. One camera at a polar angle of 0º and the second camera at a polar angle of 63.44º. With five equal turntable increments the 63.44º polar angle camera

would record five projected areas and with one projected area from the 0º polar angle camera the orientation vectors of the level 0 icosahedron are replicated.

Unfortunately, none of the cameras in the 3D imaging system have a polar angle of 63.44º. The two cameras with polar angles closest to the ideal polar angle are Cameras B and C, which have polar angles of 70.16º and 53.17º, respectively. To approximate five of the orientation vectors of the level 0 icosahedron, Cameras B and C are weighted based on their angular distance away from the ideal polar angle. To determine the weighting factor for Camera B (W_B) and Camera C (W_C) the system of equations in Eq. 4 are solved simultaneously. In Eq. 4, θ_{icos} is the ideal polar angle of a regular icosahedron (equal to 63.44º), θ_B is the polar angle of Camera B (equal to 70.16º), and θ_C is the polar angle of Camera C (equal to 53.17º).

$$W_B \times \theta_B + W_C \times \theta_C = \theta_{icos}$$
$$W_B + W_C = 1 \tag{4}$$

At each turntable increment W_B and W_C contribute one effective projected area. The last vertex of the icosahedron is represented by weighting the projected areas from Camera F with 0.2 so that for five turntable increments, the summation of $\sum_{j=1}^{5} A_{F,j}(\theta_F, \phi_j) W_F$ results in one effective projected area. Table 6 shows the resulting icosahedron weighting factor for the six cameras of the 3D imaging system.

Table 6. Icosahedron weighting factor

Camera	Weighting Factor (W)
A	0.0000
B	0.6041
C	0.3959
D	0.0000
E	0.0000
F	0.2000

To account for the fact that the summation of the weighting factor does not equal one, the projected areas are normalized by $n+0.2n$ where n is the number of turntable increments. This allows the icosahedron weighting factor to be applied to turntable increments other than five while maintaining the same ratio of effective projected areas from Cameras B, C, and F.

With the icosahedron weighting factor formulated, its effectiveness is tested in an updated emulated imaging system from [8]. In [8], the orientation vectors of the cameras were assumed to be evenly spaced between polar angles of 0º and 90º. However, the updated emulated imaging system uses the physical positions of the cameras and then generates unit orientation vectors from the camera positions. Fig. 6 shows the physical positions of the cameras (denoted as asterisks) in the 3D imaging system (with 20 turntable increments) used with the updated emulated imaging system. Each color represents one of the six cameras of the 3D imaging system. Also, the origin of the coordinate system is the center of the turntable.
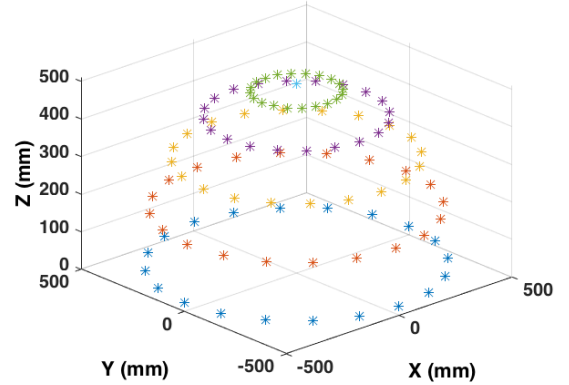

Figure 6. Emulated imaging system camera locations for 20 turntable increments

Table 7 shows the measured initial camera positions for the emulated imaging system.

Table 7. Initial camera positions in the emulated imaging system

Camera	X (mm)	Y (mm)	Z (mm)
A	498.48	0.00	23.39
B	466.37	0.00	168.26
C	404.04	0.00	302.57
D	301.80	0.00	410.69
E	151.14	0.00	480.99
F	0.00	0.00	504.41

The projected area ($A(\phi,\theta)$) of the test object is computed at each camera location and the ACSA is computed ($ACSA_C$) with Eq. 5.

$$ACSA_c = \frac{1}{n+0.2n} \sum_{j=1}^{n} \sum_{i=1}^{6} A_{i,j}(\theta_i, \phi_j) W \tag{5}$$

To test the effectiveness of the icosahedron weighting factors the following turntable increments were considered for all six test objects: 4, 8, 10, 12, 16, 20, 40, 60, 72, 80, 100, and 120. Figure 7 shows the percent error for $ACSA_C$ for the test objects at all of the turntable increments.

The main takeaway from Fig. 7 is that for low numbers of turntable increments the percent error fluctuates, but as the number of turntable increments is increased past 12 the percent error of ACSA_C essentially levels off within ±5% for all of the tested shapes. Therefore, when the icosahedron weighting factor is tested with the physical 3D imaging system the number of turntable increments tested are 12, 20, and 40.
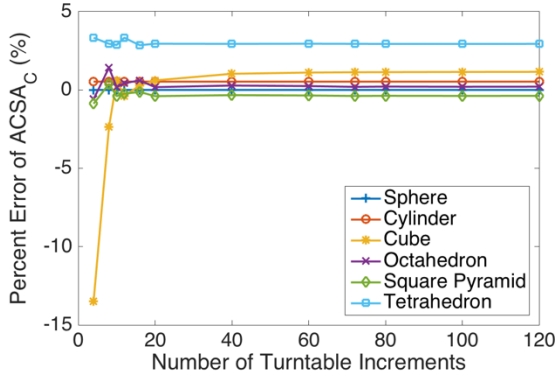
Figure 7. ACSA_C for all tested shapes and turntable increments

5 TEST RESULTS AND CONCLUSION

To test the effectiveness of calculating ACSA with the icosahedron weighting factor on physical objects the six shapes tested with the emulated imaging system were 3D printed. Since the shapes tested are convex, the true ACSA is determined as one-fourth of the total surface area of the objects. The dimensions of the objects were physically measured before calculating the total surface area of the objects. Table 8 shows the true ACSAs of the test objects used to calculate the percent error of ACSA_C from the 3D imaging system.

Table 8. True ACSA (in mm²) of test objects

Test Object	True ACSA
Sphere	700.3
Cylinder	1077
Cube	1355
Octahedron	767.5
Square Pyramid	608.6
Tetrahedron	711.3

Next, the icosahedron weighting factor was applied to projected areas recorded from the 3D imaging system in the process detailed in [8]. Note that since [8], the location of the turntable relative to the cameras was shifted and the calibration was then redone. Figure 8 shows the resulting percent errors of the ACSA_C for the tested shapes at turntable increments of 12, 20, and 40.
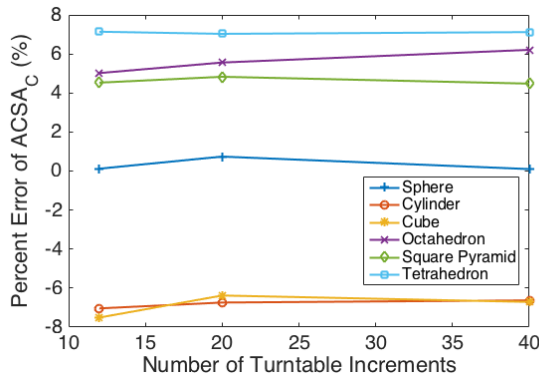

Figure 8. ACSA_C from the 3D imaging system

The main takeaway from Fig. 8 is that the magnitude of the percent error of ACSA_C is within ±8% for all of the test objects. This is larger than the errors from the emulated imaging system which means there are some errors introduced by the 3D imaging system. Also, the percent errors remain relatively constant as the number of turntable increments is increased. It is interesting that the ACSA of the test objects can be calculated only using projected area information from three of the six cameras.

To put the presented results in perspective, the percent error of the ACSA_C for the icosahedron weighting factor at 20 turntable increments is compared to the ACSA_C for the weighting factor introduced in [8] (referred to as the radial weighting factor) and the ACSA_C from the standard breakup model. All of the tested shapes fall into the irregular category, and therefore Eq. 1 is applied. However, x, y, and z (the size characteristics) must first be determined for the test objects. The size characteristics of the sphere are all equal to the diameter of the sphere (29.86 mm), but determining the size characteristics for the other test objects is more difficult. One way to determine the size characteristics of the other test objects is to use a numerical algorithm previously developed for the DebriSat project [10]. The input for the algorithm is a 3D point cloud of the object, which was numerically generated for each test object. Table 9 shows the size characteristics of the test objects.

Table 9. Size characteristics of the test objects

Test Object	x (mm)	y (mm)	z (mm)
Sphere	29.86	29.86	29.86
Cylinder	42.72	42.72	32.16
Cube	52.07	49.12	42.48
Octahedron	42.10	42.10	42.10
Square Pyramid	42.21	42.21	21.11
Tetrahedron	40.53	40.53	28.66

With the size characteristics calculated for the test objects, Eq. 1 can be applied to determine the ACSA_C of the satellite standard breakup model. Table 10 shows the percent errors of the ACSA_C for the icosahedron weighting factor, the radial weighting factor, and the satellite standard breakup model.

Table 10. Percent error of ACSA_C for all test objects

Test Object	Icosa-hedron Weighting Factor	Radial Weighting Factor	Standard Breakup Model
Sphere	0.12%	0.70%	-15.12%
Cylinder	-6.74%	-5.20%	-5.65%
Cube	-6.38%	-4.71%	12.44%
Octahedron	5.56%	3.46%	54.96%
Square	4.83%	1.66%	30.13%

Pyramid Tetrahedron	7.03%	4.48%	23.90%
Average Magnitude	5.11%	3.37%	23.70%

As can be seen in Tab. 10, the trends for the two approaches with the 3D imaging system are similar in that the sign of the percent error for the shapes are the same. When comparing the results of the icosahedron and radial weighting factors, the magnitude of the percent error with the radial weighting factor is smaller for all of the test objects except the sphere. One possible reason for the anomaly in the results of the sphere with the radial weighting factor could be due to the projected area of the sphere is constant regardless of the direction of the orientation vector; therefore, small positive errors in the projected areas measured with the 3D imaging system could be compounding since twice as many images are used with the radial weighting factor when compared to the icosahedron weighting factor. However, the small errors associated with the projected areas of the other test objects are sign indefinite and therefore with the radial weighting factor seem to contribute to a smaller overall percent error than the error introduced from not using half of the projected area information (as in the icosahedron weighting factor). Another trend evident from Tab. 10 is that both approaches with the 3D imaging system show improvement when compared to the ACSA approximation utilized in the current standard breakup model.

6   FUTURE WORKS

Work continues on the 3D imaging system for other purposes, which could result in the location of the turntable and cameras shifting again. Therefore, the weighting factors could slightly change when the locations are finalized. After all of the components are fixed the weighting factors will be recalculated if the locations shift. Also, if the locations do shift, the percent errors of the $ACSA_C$ for the weighting factors will be recalculated. Also, in this study the notional icosahedron imaging system showed promise for calculating ACSA from projected areas that are equally spaced around an object. In theory a physical system that mimics the orientation vectors of the notional icosahedron system could be built, but that is beyond the scope of this project given the results presented for the two approaches that utilize the projected areas measured with the current 3D imaging system. When moving forward with computing ACSA for the DebriSat project, the author recommends the radial weighting factor since the average magnitude of the percent error of the tested shapes is lower than the icosahedron weighting factor.

8   REFERENCES

1. Osiander, R., and Ostdick, P., Introduction to Space Debris, *Handbook of Space Engineering, Archaeologyn and Heritage*, CRC Press, Boca Raton, FL, 2009, pp. 363-379.

2. Kessler, D., and Cour-Palais, B., Collision Frequency of Artificial Satellites: The Creation of a Debris Belt, *Journal of Geophysical Research*, **83**(A6), 1978, pp. 2637-2646.

3. Englert, C., Optical Orbital Debris Spotter, *Acta Astronautica*, **104**, 2014, pp. 99-105.

4. Rivero, M., Shiotani, B., Carrasquilla, M., Fitz-Coy, N., Liou, J.-C., Sorge, M., Huynh, T., Opiela, J., Krisko, P., and Cowardin, H., DebriSat Fragment Characterization System and Processing Status, *67th IAC Congress*, Guadalajara, Mexico, 2016, IAC-16.A6.2.8x35593.

5. Slepian, Z., The Average Projected Area Theorem − Generalized to Higher Dimensions, 2011.

6. Hanada, T., and Liou, J.-C. Theoretical and Empirical Analysis of the Average Cross-sectional Areas of Breakup Fragments, *Advances in Space Research*, **47**(9), 2011, pp. 1480-1489.

7. Moraguez, M., Patankar, K., Fitz-Coy, N., Liou, J.-C., Sorge, M., Huyhn, T., Cowardin, H., Opiela, J., Krisko, P., An Imaging System for Automated Characteristic Length Measurement of DebriSat Fragments, *66th IAC Congress*, Jerusalem, Israel, 2015, IAS-15-A6.1.30288.

8. Scruggs, T., Fitz-Coy, N., Kreiter, K., Moraguez, M., Pantankar, K., Average Cross-Sectional Area of DebriSat Fragments Using Volumetrically Constructed 3D Representations, *67th IAC Congress*, Guadalajara, Mexico, 2016, IAC-16.A6.1.8.x35504.

9. Teanby, N. A., An Icosahedron-based Method for Even Binning of Globally Distributed Remote Sensing Data, *Computers & Geosciences*, **32**(9), 2006, pp. 1442-1450.

10. Moraguez, M., An Algorithm for Characteristic Length Measurement from Point Cloud Data, *AIAA Student Conference*, Savannah, GA, 2015